Pergamon

Int. J. Mech. Sci. Vol. 37, No. 11, pp. 1179–1202, 1995

0020-7403/95 $9.50 + 0.00

0020-7403(95)00016-X

TRANSIENT CREEP ANALYSIS OF BALL INDENTATION

N. OGBONNA, N. A. FLECK and A. C. F. COCKS
University Engineering Department, Trumpington Street, Cambridge, CB2 1PZ, U.K.

(*Received* 3 *May* 1994; *and in revised form* 5 *December* 1994)

Abstract—The effect of transient creep on the indentation behaviour of a creeping solid has been investigated for a strain hardening primary creep law. Numerical analyses have been performed to obtain the full field solution for a frictionless ball indenter. The functional form of the relationship between the uniaxial response of the solid and the indentation behaviour of the material is explored. The implications of the results are discussed with regard to displacement- and load- controlled indentation creep tests, and the time hardening creep law. Experiments on primary creep indentation of lead support the indentation theory.

1. INTRODUCTION

Indentation tests provide a quick, cheap and effective way of determining a range of mechanical properties of engineering materials. At elevated temperatures, tests of this type can be used to determine the creep properties of a material. The standard test involves applying a constant load to the indenter and measuring the change in the area of contact as a function of time. An indentation test can also be conducted by pressing the indenter into the material at a prescribed speed and measuring the load as a function of time. The interpretation of the results of these tests (Bower *et al.* [1]; Hill [2]; Matthews [3]; Mulhearn and Tabor [4]; Sargent and Ashby [5]) have been largely based on steady-state creep laws. Such laws are designed to predict the creep deformation of a solid subjected to a constant stress and at long times after the effects of transients arising from primary creep and stress redistribution from the elastic state become negligible.

In reality, an indentation test is a short term test with the stress state changing in magnitude and in direction at each material point during the course of a test. Clearly, it is important to employ constitutive laws that adequately describe the material response over the range of stress histories experienced by material elements during an indentation test. It is often found that the indentation test overestimates the stress exponent for power law creep; see for example Sargent and Ashby [5].

A major source of error in the interpretation of creep properties from indentation tests has been the neglect of primary creep. In the current paper, primary creep is included in a rigorous indentation analysis and tests on lead confirm the significance of primary creep. We consider the response of a creeping solid when a rigid spherical indenter is pushed into its surface. In order to address the role of transient creep, two different approaches are adopted. In the first approach, we employ the classical strain hardening primary creep law in the analysis. The structure of the strain hardening law allows the scaling procedure of Hill [2] and Bower *et al.* [1] to be extended to predict the response for this class of constitutive law. In the second approach, the indentation creep response is determined for a time hardening material. This is done simply by a suitable choice of time variable and makes direct use of the steady-state creep analysis of Bower *et al.* [1]. Of the two descriptions of creep behaviour, the strain hardening hypothesis permits a more accurate modelling of the material response, but, in general, it is easier to use the time hardening law in any component analysis. Marriott and Leckie [6] have shown that, in structural problems where the load is held constant and stress redistribution from the elastic state occurs well within primary creep, the two types of models predict comparable results. In the class of problem considered here, however, the stresses change continually throughout a test and it is instructive to examine the extent to which the time hardening law can be used to predict the component response.

2. DESCRIPTION OF PRIMARY CREEP UNDER UNIAXIAL STRESS

As a material creeps, microstructural processes which involve the generation and rearrangement of dislocations occur in the material. These changes in microstructure modify the response of the material to the applied stress. It follows that the creep rate is a function of the applied stress and the temperature in addition to the microstructural state of the material. From the physical viewpoint, the complete description of creep behaviour requires a coupled set of rate equations

$$\dot{\varepsilon} = \mathrm{f}(\sigma, T, S_i),$$
$$\dot{S}_i = \mathrm{g}_i(\sigma, T, S_k), \tag{1}$$

where S_i represents a set of macroscopic state variables which describe the microstructural state of the material. In the above equations, $\dot{\varepsilon}$ is the creep rate, σ is the stress, T is the temperature, and $\dot{S}_i$ is the time rate of change of the state variable S_i. The functions f and g_i are given by any physical model or empirical description of the creep response.

A number of state variable models with the above structure have been proposed to describe creep throughout the entire life of a component. Here, we are interested in the early stages of the creeping process and select state variables that can describe the initial shape of the creep curve. The simplest constitutive relationships with the structure Eqn (1) are the strain- and time-hardening constitutive laws. In each case, the material response is described in terms of a single state variable, with S_i being either strain ε or time t. These constitutive laws can be readily generated from a series of uniaxial creep curves obtained at different stresses, as shown schematically in Fig. 1. More elaborate models of the creeping process have been developed. Ion *et al.* [7] and Derby and Ashby [8] give models based on the different types of dislocation processes that can occur during primary creep, while empirical models have been developed by, for example, Evans and Wilshire [9], Chaboche and Rousselier [10], Pugh and Robinson [11] and Mroz and Trampczynski [12]). Each of these models are expressed in the form of Eqn (1), employing isotropic and kinematic variables to describe the material response. The single state variable models employed in the current study are isotropic in character. They do not provide the most general description of transient creep, such as the phenomenon of an incubation time under a step decrement in stress. However, they readily allow the major features of the indentation process to be identified and the influence of primary creep on the deformation response to be evaluated.

Here, we restrict our consideration to situations where, during a uniaxial creep test at constant stress, the strain rate decreases continuously throughout the primary stage of creep. Figure 1(a) shows three primary creep curves. Consider the situation where the material is allowed to creep for a time t_2 at a stress σ_2; the accumulated strain is designated ε_2. Now increase the stress to σ_3. The strain hardening hypothesis assumes that the subsequent creep response is given by translating the σ_3 creep curve horizontally until it intersects the σ_2 curve at $\varepsilon = \varepsilon_2$. This translation is shown in Fig. 1(a) and the resulting creep response is shown in Fig. 1(c). The time hardening hypothesis requires translation of the σ_3 creep curve vertically until it intersects the σ_2 curve at $t = t_2$ as shown in Fig. 1(a), with the subsequent response again indicated in Fig. 1(c). It is evident from Fig. 1(c) that the strain hardening model predicts the faster creep and, therefore a "softer" creep response. A similar argument can be constructed for a step decrease in stress. If the stress is decreased to a stress σ_1 after creeping for a time t_2 at stress σ_2, the time hardening model predicts the faster subsequent creep rate. The response resulting from a step decrease is illustrated in Fig. 1(d). This feature of the material behaviour is considered in more detail in Section 5, where we compare the indentation response resulting from the two different descriptions of the material.

Constitutive laws for primary creep typically involve either power law or exponentially decaying functions of time. A critical survey of primary creep laws has been given by Derby and Ashby [8]. In particular, the Norton–Bailey–Andrade uniaxial creep behaviour can be expressed in time hardening form as

$$\varepsilon = \varepsilon_0 \left[\left(\frac{\sigma}{\sigma_0} \right) \left(\frac{t}{t_0} \right)^M \right]^{\frac{1}{M+N}}, \quad (0 < M, N < 1), \tag{2}$$

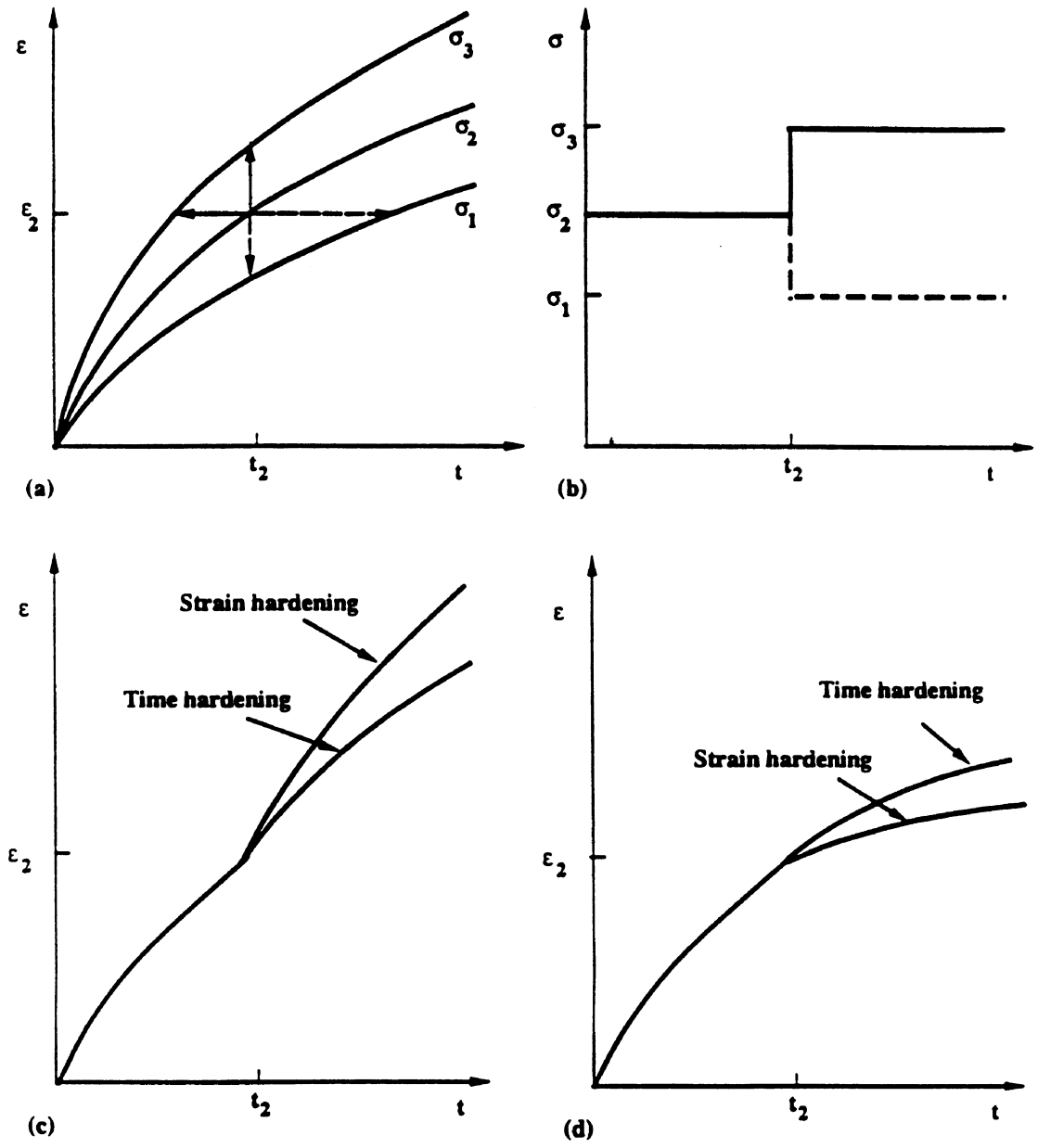

Fig. 1. Predicted response using strain- and time-hardening theories; (a) creep curves under constant stress, (b) stress histories, (c) response to step increase in load and (d) response to step decrease in load.

where ε_0 is the strain after a time t_0 at a constant stress σ_0. Leckie and Hayhurst [13] have demonstrated that, if t_0 is suitably chosen, Eqn (2) provides an appropriate description of the creep response for time varying stress states. Equation (2) can be differentiated to provide the creep rate, which we write in the following form

$$\sigma = \sigma_0 \left(\frac{\dot{\varepsilon}}{\dot{\varepsilon}_0}\right)^{M+N} \left(\frac{t}{t_0}\right)^{N}, \tag{3}$$

where $\dot{\varepsilon}_0 = (\frac{\varepsilon_0}{t_0})(\frac{M}{M+N})$. Substituting for t in Eqn (3) gives, via Eqn (2), the primary creep response under constant stress σ in the strain hardening form

$$\sigma = \sigma_0 \left(\frac{\dot{\varepsilon}}{\dot{\varepsilon}_0}\right)^{M} \left(\frac{\varepsilon}{\varepsilon_0}\right)^{N}. \tag{4}$$

Typically, M and N are taken to range from zero to unity. When $M = 0$, Eqn (4) gives the power law response of a strain hardening plastic solid; $N = 0$ corresponds to the special

case of a steady state creeping solid. Relations (3) and (4) give the same strain-time response under constant stress, but different responses under varying stress as discussed in Section 1.

3. STATEMENT OF THE PROBLEM

The following boundary value problem is considered. A frictionless rigid spherical indenter, of diameter D, is driven into a half space at a constant speed $\dot{h}$, where h is the indentation depth. The configuration is shown in Fig. 2. The half space is taken to be the strain hardening creeping solid (4). The solid is considered to be isotropic and plasticially incompressible. Under multiaxial loading relation (4) generalizes to

$$S_{ij} = \frac{2}{3}\sigma_0 \left(\frac{\varepsilon_e}{\varepsilon_0}\right)^N \left(\frac{\dot{\varepsilon}_e}{\dot{\varepsilon}_0}\right)^{M-1} \frac{\dot{\varepsilon}_{ij}^{pl}}{\dot{\varepsilon}_0}, \tag{5}$$

where a Cartesian reference frame x_i, and standard index notation, have been adopted. Here, S_{ij} is the deviatoric part of the Cauchy stress tensor and $\dot{\varepsilon}_{ij}^{pl}$ is the plastic part of the Eulerian strain rate; ε_0, $\dot{\varepsilon}_0$ and σ_0 are normalizing material constants. The effective strain rate $\dot{\varepsilon}_e$ is

$$\dot{\varepsilon}_e = \sqrt{\frac{2}{3}\,\dot{\varepsilon}_{ij}\dot{\varepsilon}_{ij}}, \tag{6}$$

and is integrated at each material point with respect to time t to give the effective strain

$$\varepsilon_e = \int \dot{\varepsilon}_e \, dt. \tag{7}$$

In this study, we use the finite element method to calculate the identation response of the half space. For computational convenience, the solid is assumed to suffer an additional elastic strain rate $\dot{\varepsilon}_{ij}^{el}$ of

$$\dot{\varepsilon}_{ij}^{el} = \frac{1+\nu}{E}\check{S}_{ij} + \frac{1-2\nu}{3E}\delta_{ij}\dot{\sigma}_{kk}, \tag{8}$$

where ν is Poisson's ratio, E is Young's modulus and $\check{S}_{ij}$ is the Jaumann stress rate measure. Before presenting the finite element analysis, a scaling procedure is used to simplify presentation of the results. Details of the method are given in Appendix A. The procedure suggests a relation between the non-dimensional load $L/\pi a^2\sigma_0$, the dimensionless punch

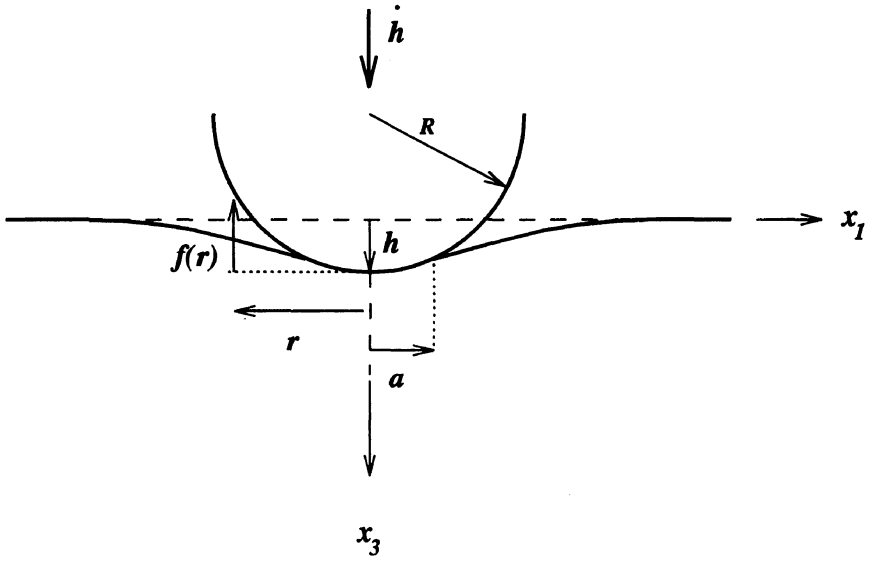

Fig. 2. Configuration for half-space indented by a rigid sphere.

velocity $h/a\dot{\varepsilon}_0$ and the non-dimensional contact radius $a/D\varepsilon_0$ of the form

$$\frac{L}{\pi a^2 \sigma_0} = F\left(\frac{\dot{h}}{a\dot{\varepsilon}_0}\right)^M \left(\frac{a}{D\varepsilon_0}\right)^N, \tag{9}$$

with the contact radius a given by

$$a = c\sqrt{Dh}. \tag{10}$$

The constants F and c are independent of punch depth and depend only upon M and N. In Eqn (9), the non-dimensional punch velocity $\frac{\dot{h}}{a}$ and the dimensionless contact radius $\frac{a}{D}$ can be regarded as appropriate average measures of the strain rate and the strain beneath the indenter. The value of c^2, obtained from Eqn (10), gives the ratio of the true to nominal contact area under the punch.

4. NUMERICAL ANALYSIS

Symmetry arguments are used to confine attention to a quarter plane, defined in cylindrical polar coordinates r and z by $(0 < r < \infty, -\infty < z < 0)$ (see Fig. 2). The finite element mesh is shown in Fig. 3. It consists of four-noded bilinear displacement, quadrilateral elements, with a relatively small number of three-noded triangular elements used for the purpose of mesh grading. All elements are axisymmetric and of the hybrid type, with independent interpolation schemes for the displacement and pressure variables to permit the modelling of incompressible behaviour. The boundary conditions on the bottom boundary are taken to be $u_z = 0$ and $\sigma_{rz} = 0$. Along $r = 0$, symmetry conditions of zero radial displacements apply. The boundary on the right-hand side is traction-free and unconstrained in either direction. The ball indenter of diameter D is modelled by a spherical rigid surface and the contact between the deforming half space and the rigid sphere is monitored using rigid surface interface elements. A preliminary convergence study showed that an element size of $0.0035D$ in the fine mesh region is adequate.

An axisymmetric finite element analysis has been performed using a commercial finite element code, ABAQUS†. The spherical indenter is pressed into the solid at a constant rate $\dot{h}$, and the indentation load L is determined as a function of time t. Since the problem is non-linear and history dependent, the solution is obtained incrementally.

The data used for the calculations are $\sigma_0/E = 10^{-3}$, $\nu = 0.3$, $\varepsilon_0 = 0.001$ and $\dot{\varepsilon}_0 = 1.0\ \mathrm{s}^{-1}$. Calculations are performed for values of the strain rate index M between 0 and 1, and for values of the strain hardening index N between 0 and 0.3. Smooth contact is assumed, and the analysis assumes finite strains and finite deformations. Details of the solution algorithm can be found in the ABAQUS reference manual.

5. FINITE ELEMENT RESULTS AND DISCUSSION

First the indentation response is given for a strain hardening solid (4) with $M = 0$ and $0 \leqslant N \leqslant 0.3$. Results are then given for a strain hardening creep solid (4) with finite M and N. These results are compared with the predictions of the more approximate time hardening creep model.

5.1. *Rate independent case*

When $M = 0$, Eqn (4) reduces to

$$\sigma = \sigma_0\left(\frac{\varepsilon}{\varepsilon_0}\right)^N, \quad (0 < N < 1), \tag{11}$$

which is constitutive relation for a strain hardening plastic solid. Numerical solutions for the indentation response of the half space have been obtained for this case using both J_2-deformation theory (non-linear hyperelastic solid) and J_2-flow theory (incremental plasticity with isotropic hardening).

† ABAQUS, version 5.2, HKS, Inc (1992).

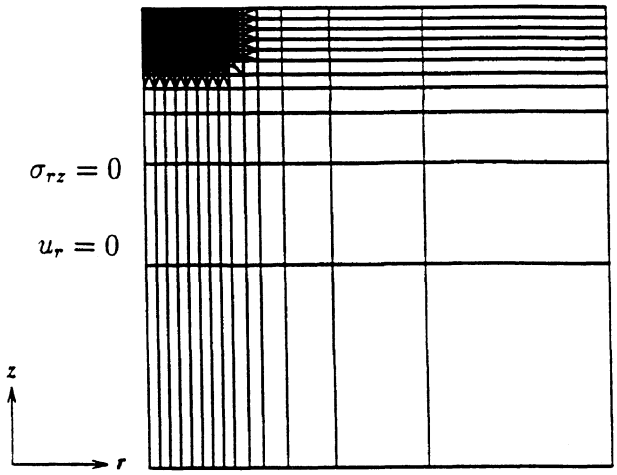

(a)

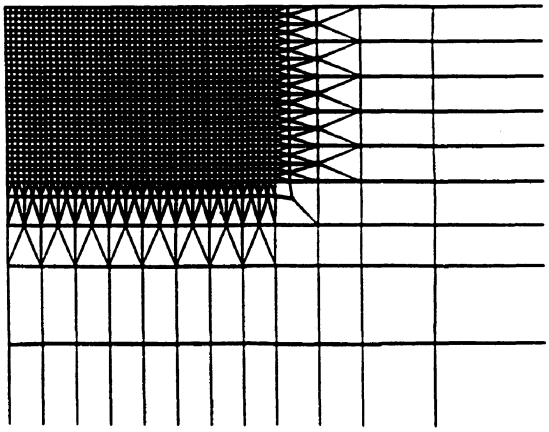

(b)

Fig. 3. Finite element mesh showing (a) boundary conditions (b) fine mesh region.

Constancy of c and F. The scaling law presented in Appendix A suggests that the load factor F and the ratio c of true to nominal contact radius are functions of the material parameters M and N only, and are independent of indentation depth. We examine the accuracy of the scaling law by comparing its predictions with the finite element calculations for both the flow theory solid and the deformation theory solid. The quantities F and c have been calculated for a range of constant size a/D using Eqns (9) and (10). Results for F are given in Fig. 4(a) and results for c are shown in Fig. 4(b). The data show a slight fluctuation for $a/D < 0.03$. As a/D increases beyond 0.03, both F and c settle to constant values. Johnson [14] has suggested that, for ball indentation of an elastic–perfectly plastic solid, the effects of elasticity may be neglected if $Ea/[D\sigma_0(1 - \nu^2)] > 25$. With regard to the present analysis, this implies that elasticity effects are negligible for $a/D > 0.025$. Thus, the initial fluctuation in the data could be due to the effects of elasticity (and also due to numerical errors in convergence). It is concluded that c and F remain essentially constant during indentation, as suggested by the scaling procedure.

Several test runs have been made using the small strain formulation within the ABAQUS program instead of the finite strain option. No significant difference in results was obtained over the range of a/D values employed in the study ($0 < a/D < 0.2$).

Indentation load and contact size. The indentation load L is of primary importance in interpreting the results of an indentation test. It is expressed in terms of the load factor F defined by Eqn (9). Numerical results for F are given in Table 1 for a range of values of N. The predictions of both deformation and flow theories are compared in Fig. 5(a). Of the two

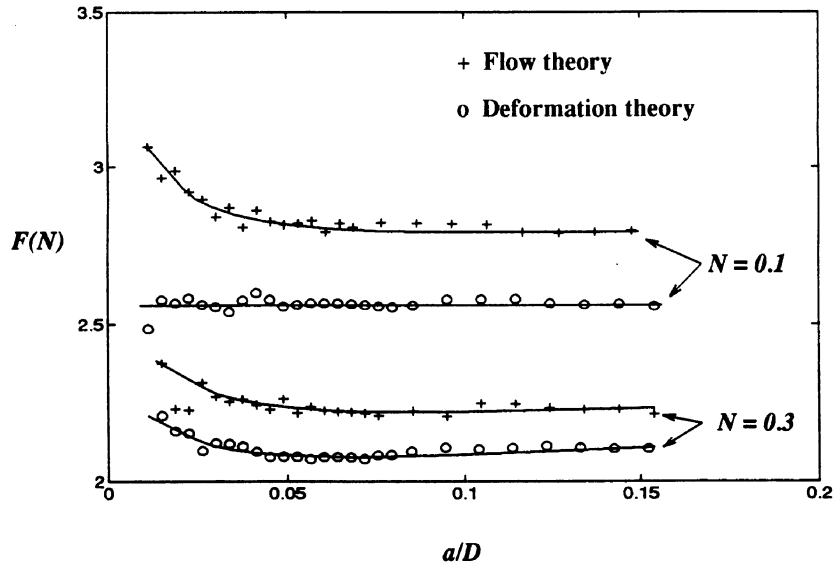

(a)

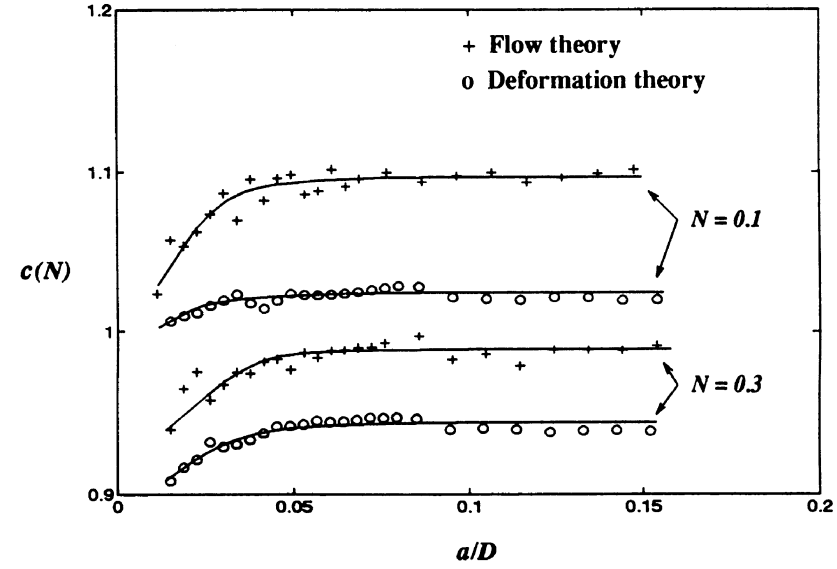

(b)

Fig. 4. Rate independent response ($M = 0$). (a) Variation of load factor F with normalized contact radius a/D. (b) Ratio of true nominal contact radius c as a function of normalized contact radius a/D.

Table 1. Results for frictionless ball indentation of a rate independent solid

	Deformation theory		Flow theory	
N	$c(N)$	$F(N)$	$c(N)$	$F(N)$
0.0	1.079	2.754	1.179	2.976
0.1	1.021	2.512	1.094	2.694
0.2	0.975	2.341	1.035	2.452
0.3	0.939	2.109	0.988	2.220
0.4	0.902	1.897	0.942	1.998
0.5	0.866	1.716	0.895	1.796
0.6	0.837	1.575	0.859	1.645
0.8	0.765	1.353	0.784	1.423
1.0	0.702	1.042	0.707	1.148

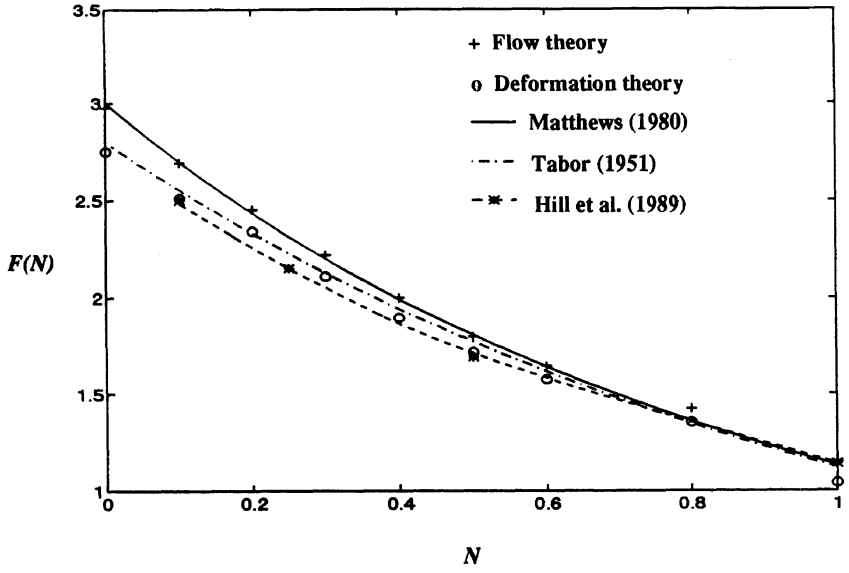

(a)

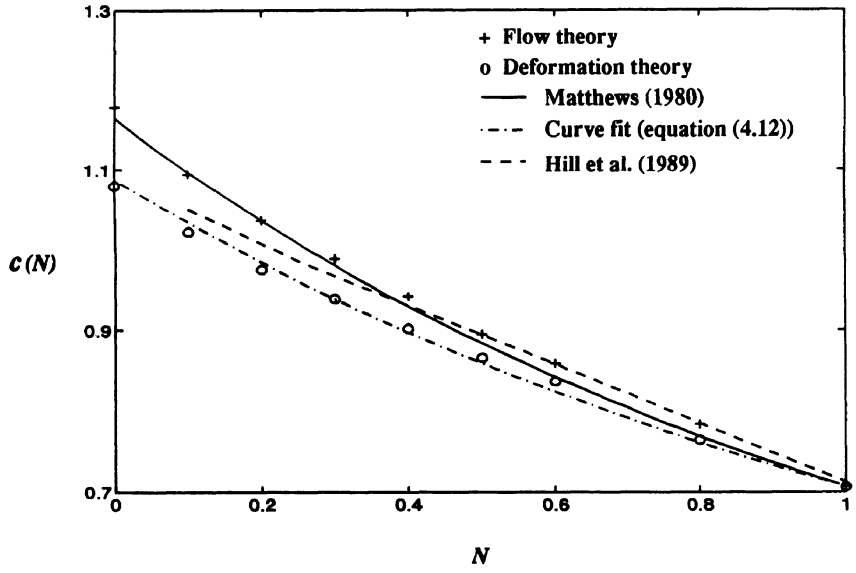

(b)

Fig. 5. Rate independent response. (a) Variation of load factor F with strain hardening index N. (b) Ratio of true to nominal contact radius c as a function of the strain hardening index N.

theories considered, the flow theory gives a slightly stiffer response, the difference being of the order of 10%. This is not surprising as the flow theory takes into account the history dependence of the response of the material while the deformation theory does not. Similar observations have been made by Ponter and Martin [15] who compared the deformation and flow theory descriptions of mechanical behaviour using extremal properties and energy theorems. They concluded that material response is stiffer for flow theory than for deformation theory when loading is non-proportional.

Hill *et al.* [16], Matthews [3] and Tabor [17] have presented solutions for the indentation load on the surface of a strain hardening solid indented by a rigid sphere. Hill *et al.* modelled the indentation response using non-linear elasticity theory. Matthews adopted a pragmatic approach and was guided by the exact solutions for a linear elastic solid and a rigid perfectly plastic material. Tabor's result was obtained by curve fitting to experimental data. For comparison, the values of F obtained from their solutions for the mean

contact pressure are also plotted in Fig. 5(a). The solutions given by Tabor and Hill *et al.* are in close agreement with the numerical results for the deformation theory solid. The response predicted by Matthews agrees with the flow theory result for all values of N, to within the numerical accuracy of the flow theory results.

It is expected that the results for the deformation theory solid are in good agreement with the calculation of Hill *et al.* [16] as the same boundary value problem is addressed in both cases. It appears that the deformation theory solid is in better agreement with the experimentally deduced result of Tabor [17] than the flow theory solid. This is consistent with the notion that the deformation theory solid is better able to capture the vertex formation on the yield surface of a polycrystalline solid (see for example Hutchinson [18]).

The relation between the contact radius a and the indentation depth h is also of interest. It has been shown that a is related to h through the constant c defined by Eqn (10). Numerical results for c are given in Table 1. The variation of c with N for the deformation theory solid and the flow theory solid is shown in Fig. 5(b) along with the values of c given by Matthews [3] and Hill *et al.* [16]. The values of c predicted by the flow theory are slightly higher than those obtained using the deformation theory. Matthews' solution is in close agreement with the flow theory results. For the deformation theory, an empirical relation is suggested for c,

$$c = \frac{1}{\sqrt{2}}\left(1 + \frac{2}{5}N\right)^{\frac{1}{N}-1}. \tag{12}$$

As seen from Fig. 5(b), Eqn (12) is an adequate approximation to the numerical results. It is exact in the limit $N = 1$ when $c = 1\sqrt{2}$.

Contact pressure profile. Representative profiles of the contact pressure are presented in Fig. 6 for $a/D = 0.1$. In this figure the pressure $p(r)$ has been normalized by the representative flow stress σ_{eff}, where

$$\sigma_{\text{eff}} = \sigma_0\left(\frac{\varepsilon_{\text{eff}}}{\varepsilon_0}\right)^N, \quad \varepsilon_{\text{eff}} = 0.4\frac{a}{D}, \tag{13}$$

and ε_{eff} is termed the representative strain beneath the indenter. Tabor [17] and Johnson [14] suggest that this choice for σ_{eff} and ε_{eff} gives an accurate estimate of the representative stress and strain beneath the indenter. The deformation theory predicts a convex shape

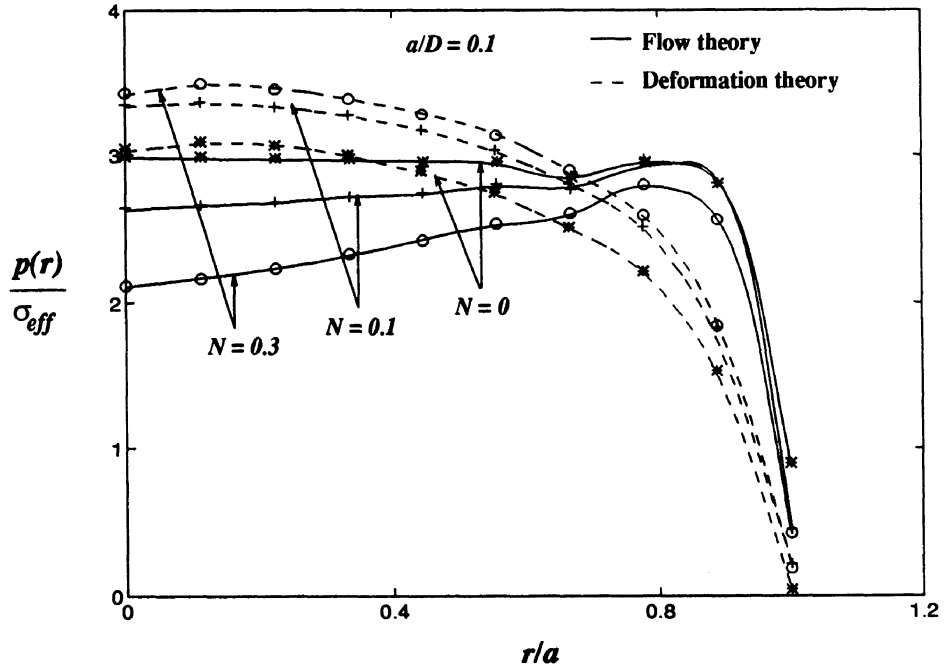

Fig. 6. Normalized contact pressure distribution $p(r)/\sigma_{\text{eff}}$ for deformation and flow theory solids. Results are shown for $a/D = 0.1$.

for the normalized pressure for all value of N, including the perfectly plastic limit ($N = 0$). In contrast, the contact pressure profiles predicted by the flow theory are flattened, the maximum pressure occurs near the edge of the contact, and lower pressures are observed towards the centre of contact than for the deformation theory solid. In particular, the ratio $p(r)/\sigma_{\text{eff}}$ is essentially constant at a value of about 3 in the limit of perfect plasticity for the flow theory solid. Finite element studies by Hardy *et al.* [19], Sinclair *et al.* [20], Yap [21] and experimental studies by Johnson [22] have shown that, for indentation of an elastic–perfectly plastic solid by a rigid punch, the contact pressure tends towards a uniform value of about 3 as the fully plastic regime is approached. While this trend is evident from the flow theory results, it is lacking in the case of a deformation theory solid.

Contours of effective and equivalent strain under the indenter. The effective strain ε_e, defined by Eqn (7), is the total accumulated plastic strain increment for a given material element. In deriving the scaling law we have used the equivalent strain $\varepsilon_{eq} = \sqrt{\frac{2}{3}\varepsilon_{ij}\varepsilon_{ij}}$, which is the magnitude of the total plastic strain. Figures 7(a)–7(c) show the contours of ε_e and ε_{eq}

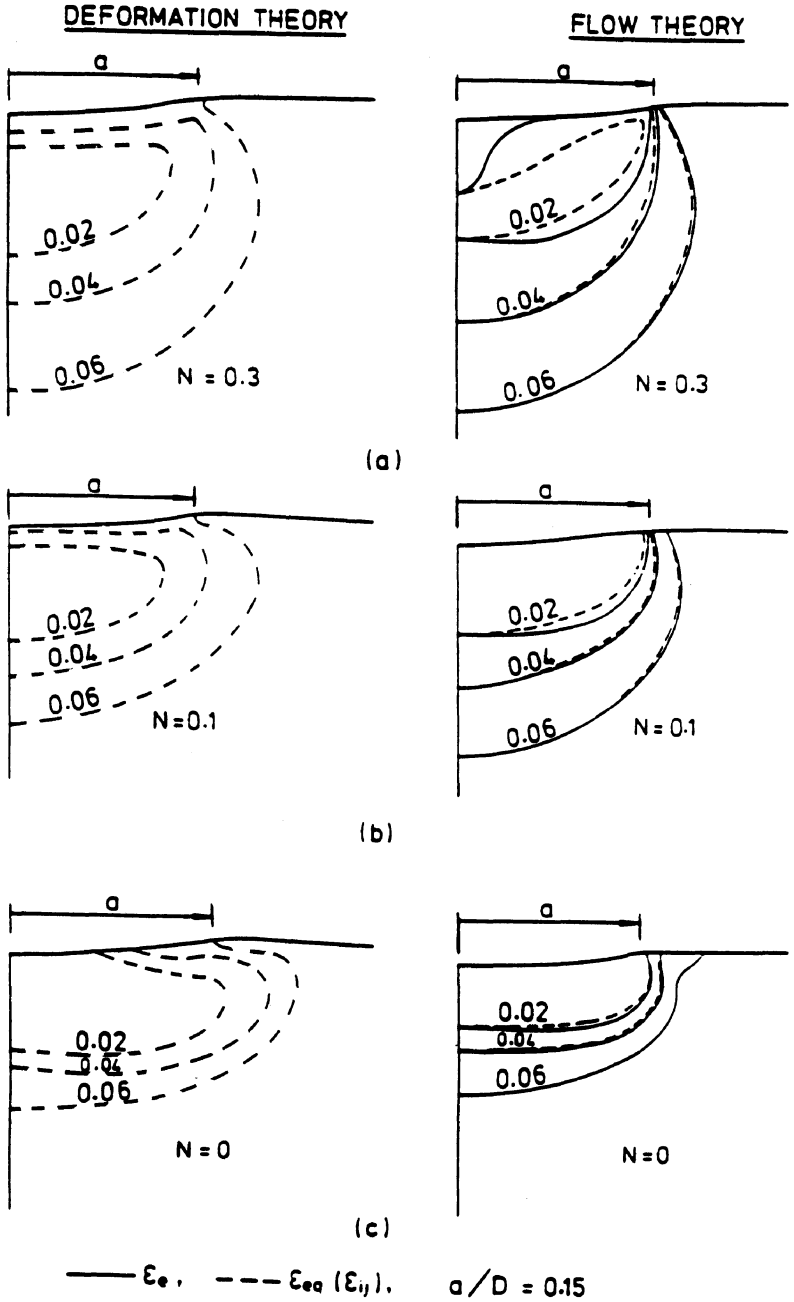

Fig. 7. Contours of ε_e and ε_{eq} for (a) $N = 0.3$, (b) $N = 0.1$ and (c) $N = 0$. Results are shown for $a/D = 0.15$.

under the indenter for $N = 0$, 0.1 and 0.3. Clearly, the strain field under the indenter is different for deformation and flow theories. For the deformation theory solid, contours of ε_{eq} are kidney-shaped, with the maximum always located on the axis of symmetry as in Hill *et al.* [16]. A local maximum in ε_e, and in ε_{eq} is observed near the edge of contact for the flow theory solid at sufficiently high values of strain hardening N: see the case $N = 0.3$ shown in Fig. 7(a). Similar observations have been made by Sinclair *et al.* [20] for an isotropic hardening flow theory solid.

The differences in behaviours of the deformation theory and flow theory solids are a consequence of non-proportional straining in the following manner. Remote from the contact region the contours of constant ε_e for the flow theory solid are close to those for constant ε_{eq}, and here the shape of the contours are similar in form to those for the deformation theory material. This reflects the near proportional stress histories experienced by elements of material in this region for both types of material. Now consider an element of material on the surface of the body at a radial distance b from the axis of symmetry. When the contact radius a is such that $a < b$, $\sigma_z = 0$ and σ_r is the maximum compressive principal stress. As the edge of the contact region passes over this point, the local stress state rotates around the yield surface until σ_z becomes the maximum compressive stress. This rotation of the stress vector in stress space occurs more abruptly for the flow theory solid, as evidenced by the contact pressure distributions of Fig. 6. This sharper transition for the flow solid is a direct result of the history dependence of the deformation process. Similar non-proportional stress histories are experienced by sub-surface elements as the edge of the contact zone passes over them. Different stress histories are required by the two different types of material to maintain compatibility of strain. As a result, the ε_e contours differ in the vicinity of contact for the two solids and the contours of constant ε_{eq} and ε_e for the flow theory solid diverge.

5.2. *Rate dependent case*

Constancy of c *and* F. The establishment of the invariance of c and F with indentation depth is essential for validation of the scaling law for the general primary creep law (5). In Fig. 8 we have plotted F and c against a/D for $M = 0.1$, 0.5 and 1, and $N = 0.1$ and 0.3. For $a/D > 0.025$, both F and c settle to reasonably constant values. The initial discrepancy in the range $a/D < 0.02$ is attributed to the effects of elasticity, and to numerical inaccuracies associated with small contact size in relation to element size. We conclude that the initial variation of F and c with a/D is due mainly to elastic effects.

Indentation load and contact size. Values for the load factor F are given in Table 2 for a range of values of M and N. The dependence of F upon M is shown in Fig. 9(a) for N in the range 0–0.3. In the limit $N = 0$, we obtain the power law viscous solution. As shown in Fig. 9(a), the calculated results are in good agreement with the values of F obtained by Bower *et al.* [1] using a different numerical procedure. For $N = 0$, the curious feature is observed that F shows a maximum at $M = 0.1$. As N increases from zero, F decreases from its steady-state creep solution and the value of M corresponding to the local maximum in F shifts towards $M = 0$. The relations (9) and (10) suggest that the mean indentation pressure $\bar{p} = L/\pi a^2$ for the primary creeping solid (4) scales with $\dot{a}/D$ and a/D according to

$$\frac{\bar{p}}{\sigma_0} = F\left(\frac{2}{c^2}\right)^M \left(\frac{\dot{a}}{D\dot{\varepsilon}_0}\right)^M \left(\frac{a}{D\varepsilon_0}\right)^N, \tag{14}$$

where F and c have already been given as functions of M and N. For ball indentation of a power law strain hardening plastic solid, Tabor [17] found that the indentation pressure $\bar{p}$ scales with a/D in accordance with

$$\bar{p} \approx 3\sigma_{\text{eff}}, \quad \sigma_{\text{eff}} = \sigma_0\left(0.4\,\frac{a}{D\varepsilon_0}\right)^N.$$

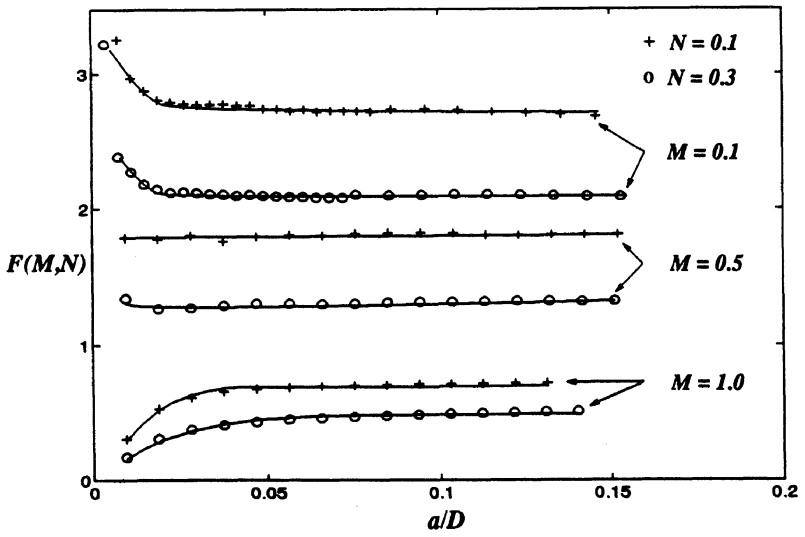

(a)

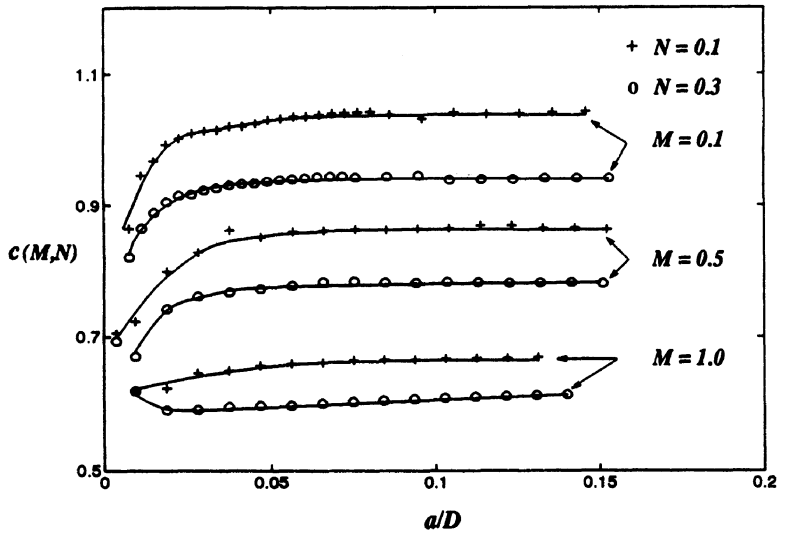

(b)

Fig. 8. Primary creep response. (a) Variation of load factor F with normalized contact radius a/D. (b) Ratio of true to nominal contact radius c as a function of normalized contact radius a/D.

Storåkers and Larsson [23] have shown that for indentation of a power law creeping solid by a sphere, $\bar{p}$ scales with $\dot{a}/D$ according to

$$\bar{p} \approx 3.33\sigma_{\text{eff}}, \quad \sigma_{\text{eff}} = \sigma_0\left(\frac{\dot{a}}{D\dot{\varepsilon}_0}\right)^M, \quad (0.125 < M < 1).$$

These considerations suggest that the indentation pressure $\bar{p}$ for the primary creeping solid is given to a good approximation by

$$\bar{p} = C_p\sigma_{\text{eff}}, \quad \sigma_{\text{eff}} = \sigma_0\left(\frac{\dot{a}}{D\dot{\varepsilon}_0}\right)^M\left(0.4\,\frac{a}{D\varepsilon_0}\right)^N, \tag{15}$$

where C_p is a constant. A comparison of Eqns (14) and (15) suggests that

$$C_p = \bar{p}/\sigma_{\text{eff}} = F\left(\frac{2}{c^2}\right)^M(0.4)^{-N}. \tag{16}$$

Table 2. Results for frictionless ball indentation of a rate dependent solid

M	N	$c(M, N)$	$F(M, N)$	C_p
	0.0	1.179	2.976	2.976
	0.1	1.094	2.694	2.953
0.0	0.2	1.035	2.452	2.945
	0.3	0.988	2.220	2.922
	0.0	1.111	3.096	3.249
	0.1	1.044	2.726	3.175
0.1	0.2	0.989	2.403	3.101
	0.3	0.940	2.097	2.995
	0.0	1.052	2.971	3.344
	0.1	0.995	2.532	3.194
0.2	0.2	0.948	2.210	3.115
	0.3	0.902	1.935	3.049
	0.0	0.905	2.177	3.402
	0.1	0.865	1.835	3.288
0.5	0.2	0.823	1.553	3.205
	0.3	0.782	1.331	3.169
	0.0	0.708	0.867	3.469
	0.1	0.666	0.726	3.588
1.0	0.2	0.637	0.585	3.463
	0.3	0.608	0.484	3.447

The calculated values of C_p are included in Table 2. C_p varies slightly with M and N, with $C_p = 3.2 \pm 0.3$. For the primary creeping solid, it appears that the approximation $\bar{p} \approx 3\sigma_{eff}$ (where σ_{eff} is defined by Eqn (15)) is accurate to within 10% for $0 \leqslant M < 1$ and $0 \leqslant N < 0.3$. By analogy with the established results for a strain hardening plastic solid (Tabor [17]) and a power law viscous solid (Storåkers and Larsson [23]), σ_{eff} may be regarded as a representative flow stress for the material under the indenter.

The contact radius a is related to the indentation depth h through the constant c defined by Eqn (10). Figure 9(b) shows the variation of c with M for various values of N. The non-dimensional contact radius c decreases with increasing values of M and N. The steady-state creep ($N = 0$) solution is an upper limit for c; the numerical results for c are in satisfactory agreement with the results obtained by Bower *et al.* [1].

Surface profile. The quantity c measures the ratio of the true to nominal contact radius. It also gives an indication of the vertical displacement of material at the edge of the contact. Material piles up at the edge of the contact if $c > 1$ and sinks in if $c < 1$. The non-dimensional surface displacement $u_3 D/a^2$ is shown in Fig. 10(a)–10(c) for a fixed contact radius $a/D = 0.1$, and for a range of values of M and N. For $M = 0$, corresponding to a rate independent strain hardening plastic solid, results are plotted in Fig. 10(a) for both the deformation and flow theory solids. Interpolation of the results shown in Fig. 10(a) for intermediate values of N shows that pile-up ($c > 1$) occurs for the flow theory solid for $N < 0.34$. For the deformation theory solid, pile-up occurs for $N < 0.26$. In general, for a given value of N the flow theory solid shows greater pile-up than the deformation theory solid.

Results for the power law viscous solid ($N = 0$) are compared with results for the flow theory plastic solid ($M = 0$) in Fig. 10(b). The surface displacement profile for the power law viscous solid at a given value of M closely resembles the profile for the rate independent flow theory solid when $N = M$. The surface profile is shown in Fig. 10(c) for the primary creeping solid (5), for N in the range 0–0.3 and M equal to 0 and 0.2. It is clear that the degree of sink-in increases with increasing N and increasing M.

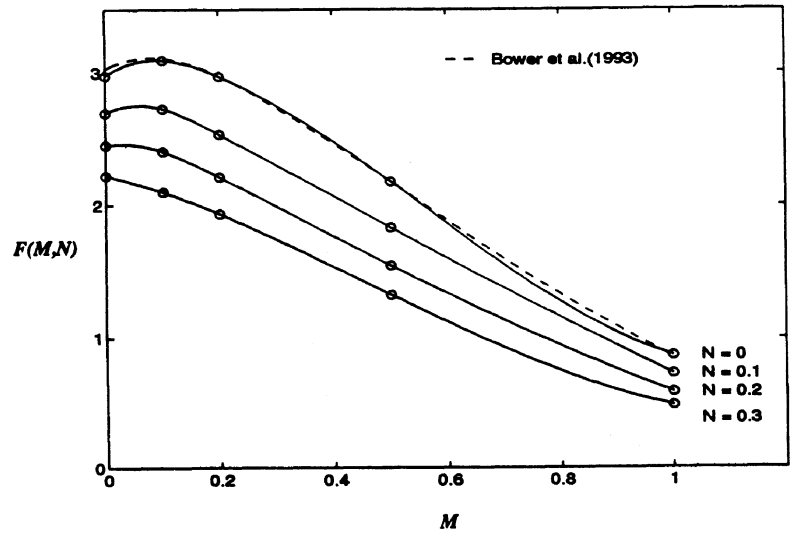

(a)

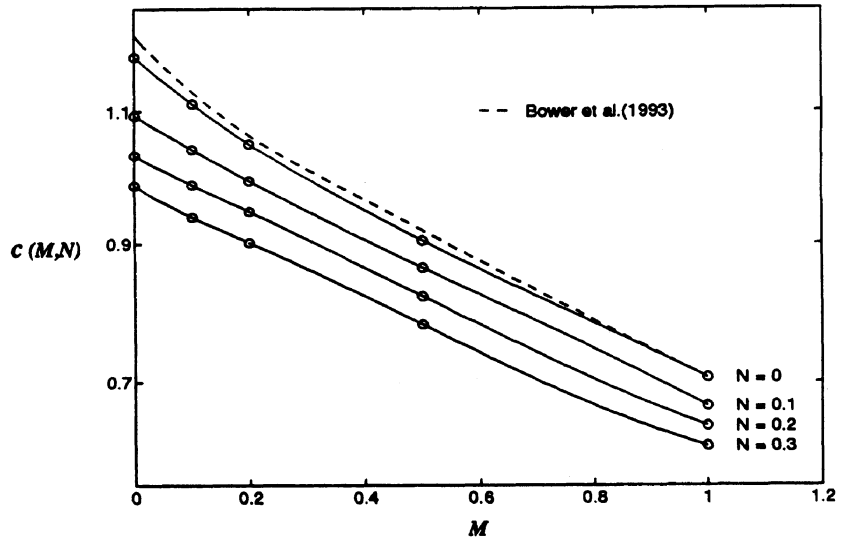

(b)

Fig. 9. Primary creep response. (a) Load factor F as a function of strain rate index M, for $N = 0$–0.3. (b) Ratio of true to nominal contact radius c as a function of strain rate index M, for $N = 0$–0.3.

Contact pressure distribution. A typical contact pressure profile is shown in Fig. 11(a) for the primary creeping solid with $M = N = 0.2$. The plot corresponds to $a/D = 0.1$ The pressure has been normalized by the representative flow stress σ_{eff} defined by Eqn (15). The profile is flattened near the centre of contact, and rises to the maximum value near the edge of contact. The results for the primary creeping solid are compared with the power law viscous solid with $M = 0.2$ and the J_2-flow theory solid with $N = 0.2$. The pressure profiles are similar in the three cases, but both the primary creeping solid and the power law creeping solid show a higher rise in pressure near the edge of contact than the flow theory solid.

A singular crack-like field exists at the edge of contact for the primary creeping solid. This has been discussed in full for the power law creeping solid (limit of $N = 0$) by Bower *et al.* [1]. The discretized nature of the finite element scheme is unable to capture the details of a singular field at the edge of the contact.

Contours of strain. Contours of constant effective strain ε_e and equivalent strain ε_{eq} for the primary creeping solid (with $M = N = 0.1$) are compared with those for the J_2-flow theory solid ($N = 0.1$) and the power law creeping solid ($M = 0.1$) (see Fig. 12). The general form of the contours is qualitatively similar for the three material models. In all cases, a local maximum in ε_e and in ε_{eq} occurs near the edge of the contact.

5.3. *Prediction of time hardening transient creep response*

The multiaxial representation of the time hardening primary creep law (3) is

$$S_{ij} = \frac{2}{3}\sigma_0 \left(\frac{t}{t_0}\right)^N \left(\frac{\dot{\varepsilon}_e}{\dot{\varepsilon}_0}\right)^{M+N-1} \frac{\dot{\varepsilon}_{ij}^{pl}}{\dot{\varepsilon}_0}, \quad (0 \leqslant M \leqslant 1;\ 0 \leqslant N \leqslant 1). \tag{17}$$

The time hardening primary creep law can be converted to a steady-state creep law by changing the time variable from t to $\tau = t^{\frac{M}{M+N}}$. Details of the procedure are given in

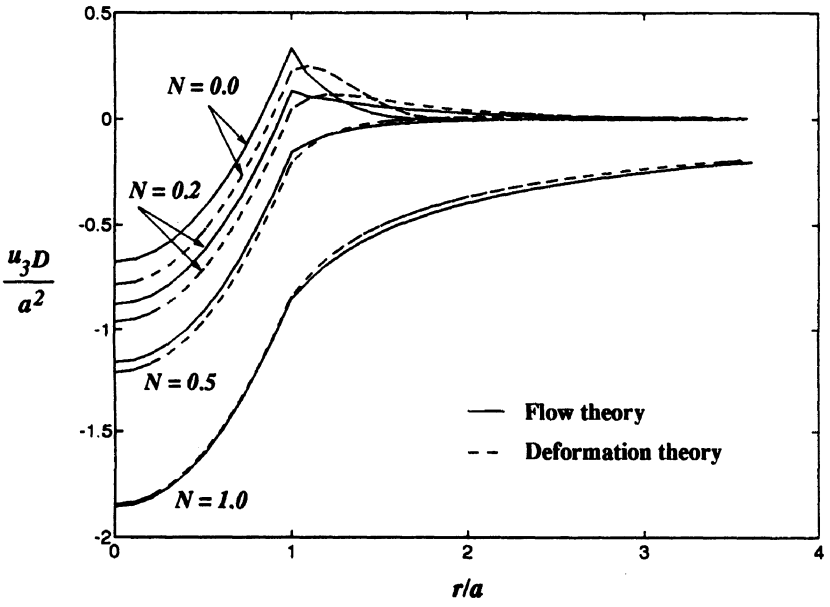

(a)

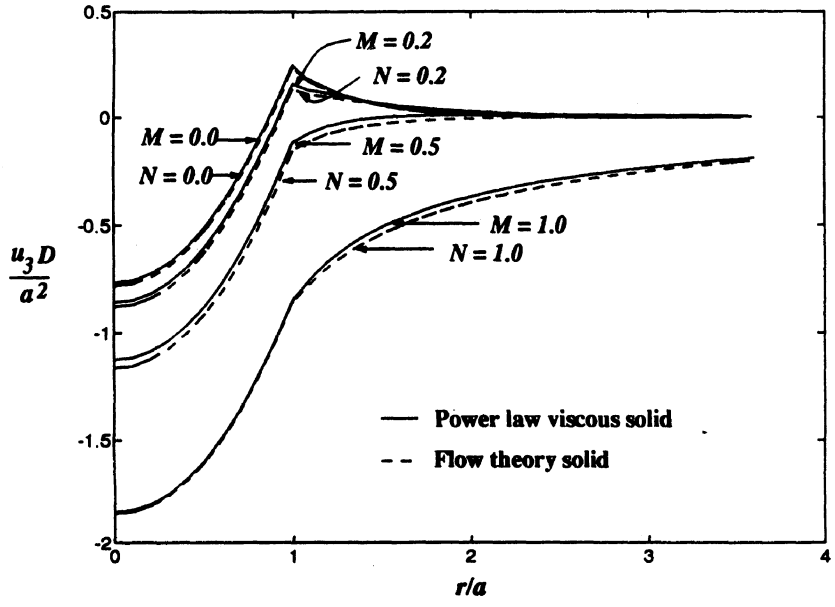

(b)

Fig. 10(a, b).

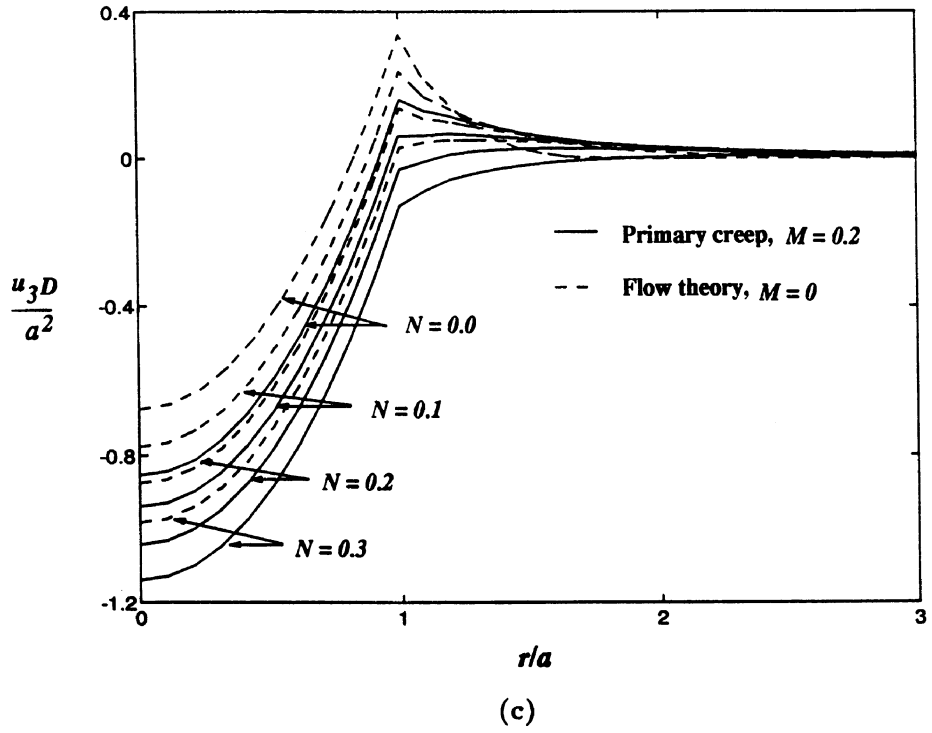

(c)

Fig. 10. Normalized normal displacement $u_3 D/a^2$ vs normalized radius r/a at $a/D = 0.1$. (a) Comparison of flow and deformation theories, rate independent case. (b) Comparison of power law viscous solid and flow theory solid. Results for the power law viscous solid are given for M values equal to the N values for the flow theory solid. (c) Comparison of profiles for a range of values of M and N.

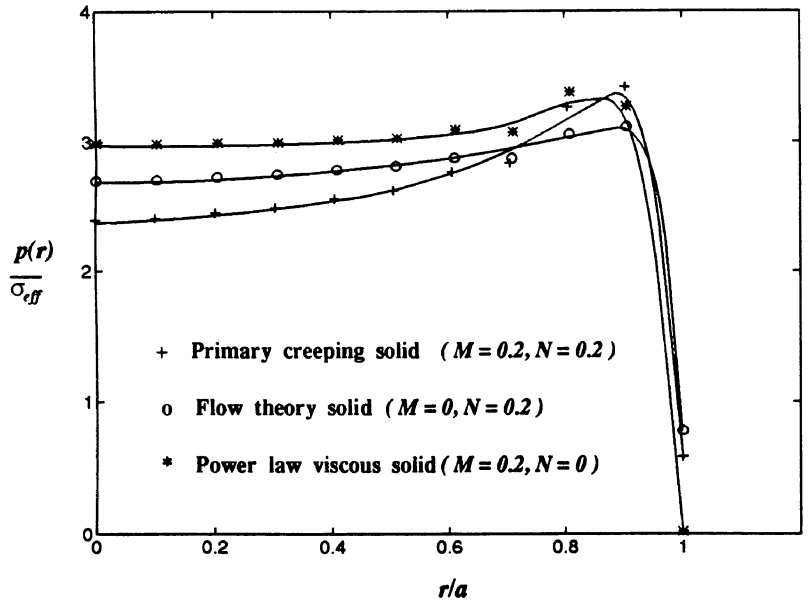

Fig. 11. Normalized contact pressure distribution $p(r)/\sigma_{eff}$ for primary creeping solid ($M = 0.2$, $N = 0.2$) is compared with the results for the power law creeping solid ($M = 0.2$, $N = 0$) and the J_2-flow theory solid ($M = 0$, $N = 0.2$). Results are shown for $a/D = 0.1$.

Appendix B. Using this method, the creep indentation behaviour of a time hardening material is obtained directly from the steady-state power law creep analysis of Bower *et al.* [1]. Results are given for both constant indentation rate $\dot{h}$ and constant indentation load L. In both cases the indentation response can be expressed in the form of Eqn (9) with

$$F = F_{ss}\left(\frac{M+N}{Mc_{ss}^2}\right)^N, \quad (M \neq 0) \tag{18}$$

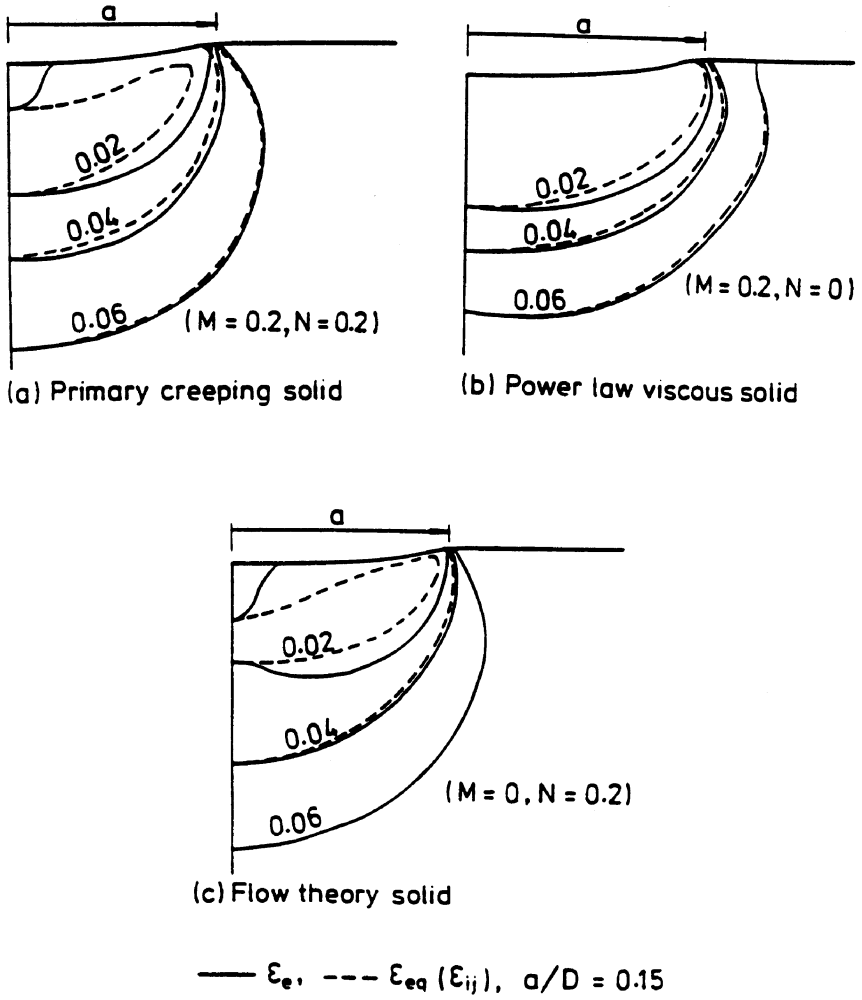

Fig. 12. Comparison of contours of the effective strain ε_e and the equivalent strain ε_{eq}: (a) primary creeping solid ($M = 0.2$, $N = 0.2$), (b) power law viscous solid ($M = 0.2$, $N = 0$) and (c) J_2-flow theory solid ($M = 0$, $N = 0.2$). Results are shown for $a/D = 0.15$.

for constant indentation rate, and

$$F = F_{ss}\left[\frac{2(M+N)}{c_{ss}^2(2+M+N)}\right]^N \tag{19}$$

for constant indentation load, as outlined in Appendix B. In the above two expressions, F_{ss} and c_{ss} refer to the load factor and non-dimensional contact radius obtained for steady state power law creep by Bower *et al.* [1], employing a creep exponent $(M + N)$.

Values of $F(M, N)$ for the two loading conditions are given in Table 3, where they are compared with predictions of the strain hardening creep law (5). The results are displayed in graphical form in Fig. 13 for $M = 0.1, 0.5$ and for several values of N. In the limit of $N = 0$, the time hardening creep law and strain hardening creep law both reduce to steady state power law creep. As N is increased from zero the results diverge, with the strain hardening material giving intermediate values of F, and the constant indentation load prediction for the time hardening solid giving the lowest load factor F. Such behaviour is expected in view of the stress history experienced by a material element during the indentation process. In a constant load test, the contact pressure decreases steadily as the contact area grows. We saw in Section 2 that if the stress on a material element is decreased, the subsequent creep rate is faster for a time hardening material than for a strain hardening one. In effect, a time hardening solid is more creep compliant during a constant load test. By a parallel argument, a time hardening solid is more creep resistant during a constant indentation rate test than a strain hardening creeping solid.

Table 3. Time hardening primary creep responses for constant load and constant indentation rate tests in comparison with the finite element (FE) results for strain hardening primary creep

		$F(M, N)$		
N	M	Constant load test (time hardening)	Constant rate test (time hardening)	Finite element analysis (strain hardening)
	0.1	3.110	3.110	3.096
0.0	0.2	2.973	2.973	2.971
	0.5	2.176	2.176	2.177
	0.1	2.507	3.147	2.726
0.1	0.2	2.390	2.840	2.532
	0.5	1.746	1.973	1.835
	0.1	2.090	3.388	2.403
0.2	0.2	1.979	2.871	2.210
	0.5	1.409	1.845	1.553
	0.1	1.773	3.817	2.097
0.3	0.2	1.653	3.011	1.935
	0.5	1.126	1.769	1.331

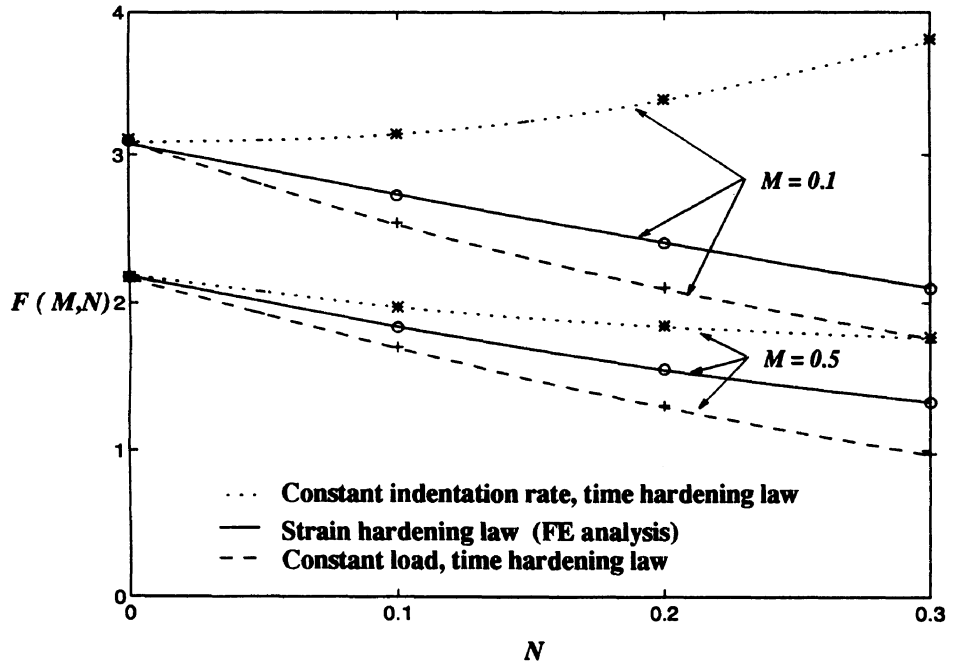

Fig. 13. Accuracy of the time hardening primary creep law compared with the strain hardening primary creep law. Effect of strain hardening index N upon load factor F for $M = 0.1$ and 0.5.

6. EXPERIMENTAL STUDY

We seek a validation of the preceding theoretical results by comparing the predictions with experimental observations. The theory emphasizes axisymmetric indentation, with particular attention to ball indentation. Only a small amount of experimental data on indentation creep by a spherical indenter was found in the literature: Mulhearn and Tabor [4], Atkins *et al.* [24] and Hill [25]; the reported data were found to be insufficient for our purpose. Therefore, primary creep indentation experiments were conducted on 99.99% pure lead using a ball indenter.

Test method

An instrumented microhardness test machine was used to measure load L as a function of indentation depth h for a spherical indenter of diameter 1 mm. Tests were performed at room temperature by applying a constant loading rate $\dot{L}$, and by continuously monitoring the indentation depth $h(t)$.

Typical indentation results in the form of $\ln(t)$ vs $\ln(h)$, at fixed $\dot{L}$, are given in Fig. 14(a). For a test performed at constant loading rate, such that $L = \dot{L}t$, the primary creep indentation theory [see Eqns (9) and (10)] suggests that the indentation depth h is related to the indentation time t by

$$t = C_1 h^{\frac{2+M+N}{2(1+M)}} \tag{20}$$

where

$$C_1 = \left[\left(\frac{2(1+M)}{2+M+N}\right)^M \left(\frac{\pi F \sigma_0}{\dot{\varepsilon}_0^M \varepsilon_0^N \dot{L}}\right)(c^2 D)^{\frac{2-M}{2}} \left(\frac{c^2}{D}\right)^{\frac{N}{2}}\right]^{\frac{1}{1+M}}. \tag{21}$$

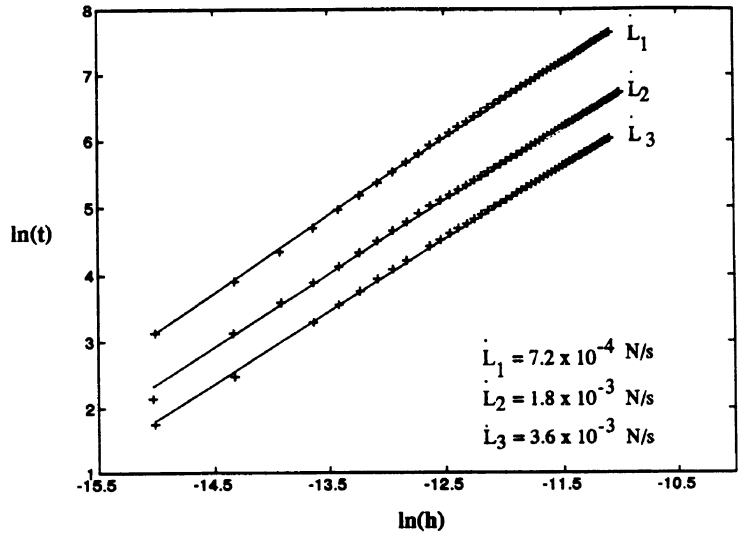

(a)

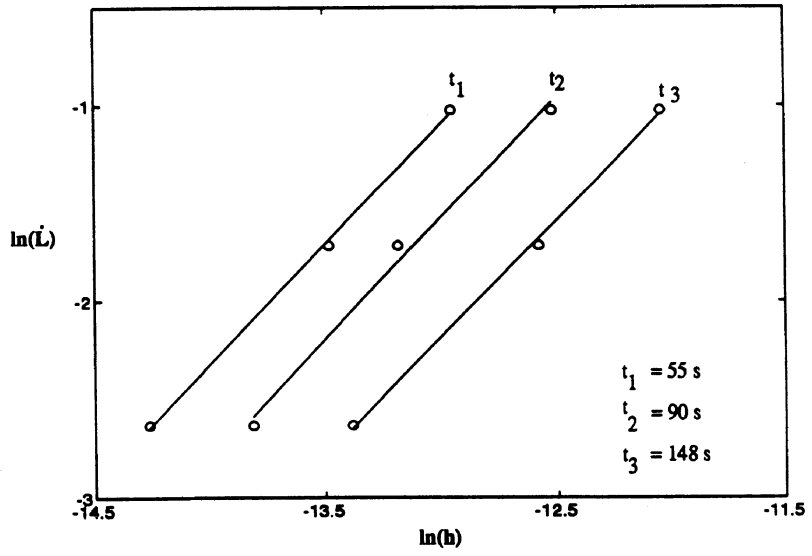

(b)

Fig. 14. Results for primary creep indentation of lead. (a) Plots of $\ln(t)$ vs $\ln(h)$ at fixed loading rate $\dot{L}$. (b) Plots of $\ln(\dot{L})$ vs $\ln(h)$ at fixed time t.

Thus, a log–log plot of t vs h (at fixed $\dot{L}$) is predicted to be a straight line of slope $\frac{2+M+N}{2(1+M)}$. This is verified by the experimental data shown in Fig. 14(a). It remains to extract the values of M and N. In order to do this, we cross-plot the data of Fig. 14(a) to give the dependence of indentation depth h upon loading rate $\dot{L}$ at fixed time. Upon re-arranging Eqns (20) and (21) we get

$$\dot{L} = C_2 h^{\frac{1}{2}(2+M+N)}, \tag{22}$$

where

$$C_2 = \left(\frac{2(1+M)}{2+M+N}\right)^M \left(\frac{\pi F \sigma_0}{\dot{\varepsilon}_0^M t^M \varepsilon_0^N}\right)(c^2 D)^{\frac{2-M}{2}} \left(\frac{c^2}{D}\right)^{\frac{N}{2}}. \tag{23}$$

Thus, a log–log plot of $\dot{L}$ vs h (at fixed time t) is predicted to be a straight line of slope $(2 + M + N)/2$. The experimental data for lead supports this prediction, see Fig. 14(b). By taking the average slopes for the plots of each figure, we find that $M = 0.097 \pm 0.012$ and $N = 0.34 \pm 0.05$. The results indicate that the material experiences significant primary creep during a test.

The value of the steady state power law creep exponent M falls within the range $M = 0.083$–0.12, according to other workers (Mulhearn and Tabor [4]; Mayo and Nix [26]; De La Torre *et al.* [27]) who have investigated the indentation creep of lead at temperatures $\geqslant 0.5 T_m$, where T_m is the melting temperature. These values are about 30% lower than the uniaxial creep exponents of $M = 0.13$ to 0.14 reported in the literature for power law creep of lead at room temperature (Frost and Ashby [28]; Akisanya and Fleck [29]). At least, part of the discrepancy may be due to the fact that primary creep occurs during an indentation test.

7. CONCLUDING DISCUSSION

The primary creep behaviour of a solid has been examined for indentation by a frictionless rigid sphere. Full account is taken of the variable stress state which exists in the material under the indenter. A functional form has been obtained for the contact size and the indentation load as a function of indentation depth and indentation rate. The analysis shows that primary creep has a significant influence on the indentation load as well as on the surface displacement profile near the indenter. For a fixed value of M, sink-in at the edge of contact becomes more pronounced as N increases from zero.

For the rate independent case, a significant difference is observed between the predictions for the deformation solid and the flow theory solid. The indentation load is 10% higher for the flow theory solid than for the deformation theory solid. This is due to non-proportional strain beneath the indenter.

Indentation creep tests at room temperature show that lead undergoes primary creep. Its creep parameters have been extracted successfully using the primary creep indentation theory.

REFERENCES

1. A. F. Bower, N. A. Fleck, A. Needleman and N. Ogbonna, Indentation of a power law creeping solid. *Proc. Roy. Soc . Lond* **A441**, 97–123 (1993).
2. R. Hill, Similarity analysis of creep indentation tests. *Proc. Roy. Soc. Lond.* **A436**, 617–630 (1992).
3. J. R. Matthews, Indentation hardness and hot pressing. *Acta Metall.* **28**, 311–318 (1980).
4. T. O. Mulhearn and D. Tabor, Creep and hardness of metals: a physical study. *J. Inst. Metals* **89**, 7–12 (1960).
5. P. Sargent and M. F. Ashby, Indentation creep. *Mater. Sci. Tech.* **8**, 594–601 (1992).
6. D. L. Marriott and F. A. Leckie, Some observations on the deflection of structures during creep. *Proc. Instn Mech. Engnrs* **178** (Pt. 3L), 115–125 (1964).
7. J. C. Ion, A. Barbosa, M. F. Ashby, B. F. Dyson and M. McLean, The modelling of creep for engineering design—I. Technical Report Dma A1115. National Physical Laboratory (1986).
8. B. Derby and M. F. Ashby, A microstructural model for primary creep. *Acta Metall.* **35**(6), 1349–1353 (1987).
9. R. W. Evans and B. Wilshire *Creep of Metals and Alloys.* Institute of Metals, London (1982).
10. J. L. Chaboche and G. Rousselier, On the plastic and viscoplastic constitutive equations Part I–Rules developed with internal variable concept. *Trans ASME, J. Pressure Vessel Technology* **105**, 153–158 (1983).

11. C. E. Pugh and D. N. Robinson, *Nucl. Engng & Design* **48**, 269–276 (1978).
12. Z. Mroz and Trampczynski, On the creep hardening rule for metals with a memory of maximal prestress. *Int. J. Solids Struct.* **20**, 467–486 (1984).
13. F. A. Leckie and D. R. Hayhurst, Creep rupture of structures. *Proc. Roy. Soc. Lond.* **A340**, 323–347 (1974).
14. K. L. Johnson, *Contact Mechanics*. Cambridge University Press (1985).
15. A. S. Ponter and J. B. Martin, Some extremal properties and energy theorems for inelastic materials and their relationship to the deformation theory of plasticity. *J. Mech. Phys. Solids* **20**, 281 (1972).
16. R. Hill, B. Storåkers and A. B. Zdunek, A theoretical study of the Brinell hardness test. *Proc. Roy. Soc. Lond.* **A423**, 301–330 (1989).
17. D. Tabor, *Hardness of Metals*. Clarendon Press, Oxford (1951).
18. J. W. Hutchinson, Plastic buckling, in *Advances in Applied Mechanics*, pp. 67–144. Academic Press (1974).
19. C. Hardy, C. N. Baronnet and G. V. Tordion, The elasto-plastic indentation of a half-space by a rigid sphere. *Int. J. Num. Meth. Engng* **3**, 451–462 (1971).
20. G. B. Sinclair, P. S. Follansbee and K. L. Johnson, Quasi-static normal indentation of an elasto-plastic half-space by a rigid sphere II. *Int. J. Solids Struct.* **21** (8), 865–888 (1985).
21. W. K. Yap, Numerical analysis of indentation of strain-hardening materials. Ph.D Thesis, University of Cambridge, U.K. (1992).
22. K. L. Johnson, An experimental determination of the contact stresses between plastically deformed cylinders and spheres, in *Engineering Plasticity* (edited by J. Heyman and F. A. Leckie) pp. 341–361 (1968).
23. B. Storåkers and P. Larsson, On Brinell and Boussinesq indentation of creeping solids. *J. Mech. Phys. Solids* **42** (2), 307–332 (1994).
24. A. G. Atkins, A. Silverio and D. Tabor, Indentation hardness and the creep of solids. *J. Inst. Metals* **94**, 369–378 (1966).
25. A. D. Hill, Modelling and assessment of diffusion bonding. Ph.D Thesis, University of Cambridge (1984).
26. M. J. Mayo and W. D. Nix, A micro-indentation study of superplasticity in Pb, Sn, and Sn-38 wt% Pb. *Acta Metall.* **36**(8), 2183–2192 (1988).
27. A. De La Torre, P. Adeva and M. Aballe, Indentation creep of lead and lead–copper alloys. *J. Mater. Sci.* **26**, 4351–4354 (1991).
28. H. J. Frost and M. Ashby, *Deformation Mechanism Maps*. Pergamon Press, Oxford (1982).
29. A. R. Akisanya and N. A. Fleck, Fatigue and creep of a constrained metal wire. *Acta Metall. Mater.* **41** (1) 121–131 (1993).

APPENDIX A: THE SCALING LAW

Hill *et al.* [16] have shown that a self-similarity principle exists for ball indentation of a power law hardening J_2-deformation theory solid. The similarity principle was extended by Hill [2] for a power law creeping solid. In this appendix the similarity principle is developed for a particular multiaxial generalization of the primary creep law (4).

A characteristic feature of ball indentation is the non-linear growth of the contact radius a with indentation depth h. The displacement u_i, strain ε_{ij} and stress field σ_{ij} are functions of a for a strain hardening solid, and functions of a and $\dot{a}$ for a creeping solid. We shall show that, for a particular change of variables, it is possible to map these evolving fields to a time invariant self-similarity solution which is independent of indentation size. The similarity principle assumes that displacements and strains remain small during the indentation process.

With respect to a Cartesian reference frame x_i, the displacement u_i, strain ε_{ij} and stress σ_{ij} in a creeping half space with constitutive law (5) satisfy the strain–displacement relation

$$\varepsilon_{ij} = \frac{1}{2}(u_{i,j} + u_{j,i}) \tag{A1}$$

and the equilibrium relation

$$\sigma_{ij,j} = 0 \tag{A2}$$

where $(\ )_{,j}$ denotes differentiation with respect to x_j in the usual manner. Now consider indentation of the solid (5) by a rigid frictionless ball at a constant indentation velocity $\dot{h}$. At the current instant the indentation depth is h and the contact radius is a. Over the contact region with the ball, the surface of the half space is displaced vertically a distance $u_3 = h - \mathrm{f}(r)$, where h is the indentation depth and $\mathrm{f}(r)$ is the head shape of the indenter (see Fig. 2). The sphere of diameter D is approximated by a parabola, giving $\mathrm{f}(r) = r^2/D$ at any radius r from the axis of symmetry. On the surface of the half space, it is required that

$$u_3 = h - \frac{r^2}{D}, \quad \dot{u}_3 = \dot{h}, \quad (r \leqslant a) \tag{A3}$$

$$\sigma_{13} = \sigma_{23} = 0, \quad (r \leqslant a) \tag{A4}$$

$$\sigma_{i3} = 0, \quad (r > a), \quad (i = 1, 2, 3). \tag{A5}$$

The above traction boundary conditions state that the ball is frictionless and that the surface is traction-free beyond the contact region. Now scale the variables x_i, r, and u_i as

$$x_k = a\tilde{x}_k, \quad r = a\tilde{r}, \quad u_i = \frac{a^2}{D}\tilde{u}_i, \tag{A6}$$

and assume that the scale variables $(\tilde{\ })$ are independent of time. The displacement rate $\dot{u}_i$ may be rewritten in scaled variables as

$$\dot{u}_i = \frac{2a\dot{a}}{D}\tilde{u}_i + \frac{a^2}{D}\frac{\partial \tilde{u}_i}{\partial \tilde{x}_k}\left(\frac{-\dot{a}\tilde{x}_k}{a}\right),$$

or, in more compact notation, as

$$\dot{u}_i = \frac{a}{D}\dot{a}\hat{u}_i, \tag{A7}$$

where

$$\hat{u}_i = 2\tilde{u}_i - \tilde{x}_k\frac{\partial \tilde{u}_i}{\partial \tilde{x}_k}. \tag{A8}$$

The strain field ε_{ij} scales as

$$\varepsilon_{ij} = \frac{a}{D}\tilde{\varepsilon}_{ij}, \tag{A9}$$

where

$$\tilde{\varepsilon}_{ij} = \frac{1}{2}\left(\frac{\partial \tilde{u}_i}{\partial \tilde{x}_j} + \frac{\partial \tilde{u}_j}{\partial \tilde{x}_i}\right), \tag{A10}$$

and the strain rate field $\dot{\varepsilon}_{ij}$ scales as

$$\dot{\varepsilon}_{ij} = \frac{\dot{a}}{D}\hat{\varepsilon}_{ij}, \tag{A11}$$

where

$$\hat{\varepsilon}_{ij} = \tilde{\varepsilon}_{ij} - \tilde{x}_k\frac{\partial \tilde{\varepsilon}_{ij}}{\partial \tilde{x}_k}. \tag{A12}$$

The displacement boundary condition (A3) over the contact region becomes

$$\frac{a^2}{D}\tilde{u}_i = h - \frac{a^2}{D}\tilde{r}^2, \quad (a\tilde{r} \leqslant a)$$

or

$$\tilde{u}_3 = \frac{1}{c^2} - \tilde{r}^2, \quad (\tilde{r} \leqslant 1) \tag{A13}$$

where

$$c^2 = \frac{a^2}{Dh}. \tag{A14}$$

Equation (A13) and the relation (A8) imply that

$$\hat{u}_3 = \frac{2}{c^2}, \quad (\tilde{r} \leqslant 1). \tag{A15}$$

The velocity boundary condition (A3) over $r \leqslant a$ may be rewritten as

$$\dot{h} = \frac{a\dot{a}}{D}\hat{u}_3. \tag{A16}$$

Note that Eqns (A14–A16) imply that c^2 is a constant and independent of time.

Now take a particular form of the multi-axial generalization of the constitutive law (4)

$$S_{ij} = \frac{2}{3}\sigma_0\left(\frac{\varepsilon_{eq}}{\varepsilon_0}\right)^N\left(\frac{\dot{\varepsilon}_e}{\dot{\varepsilon}_0}\right)^{M-1}\frac{\dot{\varepsilon}^{pl}_{ij}}{\dot{\varepsilon}_0}, \tag{A17}$$

where the equivalent strain ε_{eq} is

$$\varepsilon_{eq} = \left(\frac{2}{3}\varepsilon_{ij}\varepsilon_{ij}\right)^{\frac{1}{2}}, \tag{A18}$$

and the effective strain rate $\dot{\varepsilon}_e$ is

$$\dot{\varepsilon}_e = \left(\frac{2}{3}\dot{\varepsilon}_{ij}\dot{\varepsilon}_{ij}\right)^{\frac{1}{2}}. \tag{A19}$$

Note that $\varepsilon_{eq} = \int \dot{\varepsilon}_e \, dt$ for a material point only for the case of proportional loading. The constitutive law (A17) may be rewritten in terms of the transformed variables as

$$\tilde{S}_{ij} = \frac{2}{3}\tilde{\varepsilon}_{eq}^{N}\hat{\varepsilon}_e^{M-1}\hat{\varepsilon}_{ij}, \tag{A20}$$

where

$$\tilde{S}_{ij}(\tilde{x}_k) = \sigma_0^{-1}\left(\frac{a}{\varepsilon_0 D}\right)^{-N}\left(\frac{\dot{a}}{\dot{\varepsilon}_0 D}\right)^{-M} S_{ij}(x_k, a), \tag{A21}$$

and

$$\tilde{\varepsilon}_{eq} = \left(\frac{2}{3}\tilde{\varepsilon}_{ij}\tilde{\varepsilon}_{ij}\right)^{\frac{1}{2}} = \frac{D}{a}\varepsilon_{eq} = \frac{D}{a}\left(\frac{2}{3}\varepsilon_{ij}\varepsilon_{ij}\right)^{\frac{1}{2}}, \tag{A22}$$

$$\hat{\varepsilon}_e = \left(\frac{2}{3}\hat{\varepsilon}_{ij}\hat{\varepsilon}_{ij}\right)^{\frac{1}{2}} = \frac{D}{a}\dot{\varepsilon}_e = \frac{D}{a}\left(\frac{2}{3}\dot{\varepsilon}_{ij}\dot{\varepsilon}_{ij}\right)^{\frac{1}{2}}. \tag{A23}$$

Thus, the boundary value problem in the transformed space ($\tilde{x}_i$, $\tilde{u}_i$, $\tilde{\varepsilon}_{ij}$, $\tilde{\sigma}_{ij}$,) consists of applying a displacement given by (A13) over a fixed contact region $\tilde{r} \leqslant 1$. The usual small strain–displacement relations (A10) and the equilibrium relations (A1) are obeyed by the ($\tilde{}$) variables; the associated constitutive law is given by Eqn (A17).

In physical space, the indentation load L is obtained by integrating the contact pressure $p(r)$ over the contact region $r \leqslant a$. Thus,

$$L = 2\pi\int_0^a p(r) r \, dr.$$

If $\tilde{p}(\tilde{r})$ is the pressure corresponding to the stress field $\tilde{S}_{ij}$, then the structure of equation (A21) suggests that the mean contact pressure scales as:

$$\frac{L}{\pi a^2} = \sigma_0 F(M, N)\left(\frac{a}{\varepsilon_0 D}\right)^{N}\left(\frac{\dot{a}}{\dot{\varepsilon}_0 D}\right)^{M}, \tag{A24}$$

where

$$F(M, N) = 2\int_0^1 \tilde{p}(\tilde{r})\tilde{r} \, d\tilde{r} \tag{A25}$$

is the mean contact pressure in the non-dimensional space $\tilde{x}_i$. We conclude that the indentation load scales as (A24) and the contact radius a scales as (A14).

In principle the boundary value problem in the scaled variables could be solved in order to extract the eigenvalues c and F. In practice, it is easier to solve the physical problem directly by the finite element method, and to exploit the scaling relations (A14) and (A24) in presentation of the results.

Note that the constitutive laws (5) and (A17) are slightly different from each other. Equation (5) involves the effective strain ε_e defined by time integration of the effective strain rate $\dot{\varepsilon}_e$. On the other hand, the constitutive law (A17) in the similarity principle makes use of the equivalent strain $\varepsilon_{eq} = (\frac{2}{3}\varepsilon_{ij}\varepsilon_{ij})^{\frac{1}{2}}$ which is equal to ε_e only in the case of proportional loading. Nevertheless, we find that the scaling laws (A14) and (A24) hold to acceptable accuracy for the standard constitutive law (5) used in the finite element calculations.

APPENDIX B: THE TIME HARDENING MATERIAL

If the time variable is changed to $\tau = t^{\frac{M}{M+N}}$, the uniaxial time hardening law (3) in Section 2 reduces to a steady-state uniaxial creep law

$$\sigma = \sigma_0\left(\frac{\dot{\varepsilon}}{\dot{\varepsilon}_0}\right)^{M+N}, \tag{B1}$$

where $(') \equiv \frac{\partial}{\partial\tau}$ and τ becomes the new time variable. Relation (B1) is the standard power law creep law with exponent $(M + N)$. Thus, steady state creep analysis may be used directly to predict the response under time hardening primary creep. The power law creep indentation response given by Bower *et al.* [1] may be recast as

$$\frac{L}{\pi a^2 \sigma_0} = F_{ss}\left(\frac{\dot{h}}{a\dot{\varepsilon}_0}\right)^{M+N}. \tag{B2}$$

In Eqn (B2), F_{ss} is the steady-state value of the load factor F and $\dot{\bar{h}}$ is the rate of change of indentation depth h with respect to time τ. In physical space, the indentation depth varies with time t at a speed $\dot{h}$ which is related to $\dot{\bar{h}}$ by

$$\dot{\bar{h}} = \dot{h}\left(\frac{M+N}{M}\right)t^{\frac{N}{M+N}}. \tag{B3}$$

Also, the constant strain rate $\dot{\varepsilon}_0$ in physical space is related to $\dot{\varepsilon}_0$ by

$$\dot{\varepsilon}_0 = \dot{\varepsilon}_0\left(\frac{M+N}{M}\right)t_0^{\frac{N}{M+N}} \tag{B4}$$

Substituting for $\dot{\bar{h}}$ and $\dot{\varepsilon}_0$ in Eqn (B2) gives

$$\frac{L}{\pi a^2\sigma_0} = F_{ss}\left(\frac{\dot{h}}{a\dot{\varepsilon}_0}\right)^{M+N}\left(\frac{t}{t_0}\right)^N. \tag{B5}$$

Predictions of the indentation creep response are now given for time hardening behaviour under (i) constant indentation rate $\dot{h}$ and (ii) constant indentation load L.

(i) *Constant indentation rate test*

In a constant indentation rate test the indenter penetrates the solid to a prescribed depth h at a constant speed $\dot{h}$, so that $t = h/\dot{h}$. Substituting for t in Eqn (B5), noting from Section 2 that $t_0 = (\frac{M}{M+N})(\frac{\varepsilon_0}{\dot{\varepsilon}_0})$, and making use of Eqn (10), the transient creep response is obtained as

$$\frac{L}{\pi a^2\sigma_0} = F_{ss}\left(\frac{M+N}{Mc_{ss}^2}\right)^N\left(\frac{\dot{h}}{a\dot{\varepsilon}_0}\right)^M\left(\frac{a}{D\varepsilon_0}\right)^N, \tag{B6}$$

where c_{ss} is the steady-state value of c given by Bower *et al.* [1]. By comparison with Eqn (9), the load factor F is given by

$$F = F_{ss}\left(\frac{M+N}{Mc_{ss}^2}\right)^N, \quad (M \neq 0). \tag{B7}$$

(ii) *Constant indentation load test*

In this case, the load is kept constant while the speed of the indenter $\dot{h}$ varies. Equation (B5) must first be integrated over time before t is estimated. On noting that $\dot{h}/a = 2\dot{a}/Dc^2$ and $\dot{\varepsilon}_0 = (\frac{M}{M+N})\varepsilon_0/t_0$, integration of Eqn (B5) gives

$$\frac{t}{t_0} = \left(\frac{L}{\pi a^2\sigma_0 F_{ss}}\right)^{\frac{1}{M}}\left[\frac{2(M+N)}{c^2(2+M+N)}\left(\frac{a}{D\varepsilon_0}\right)\right]^{\frac{M+N}{M}}. \tag{B8}$$

Upon substituting (B8) into Eqn (B5), the expression for the indentation response is

$$\frac{L}{\pi a^2\sigma_0} = F_{ss}\left[\frac{2(M+N)}{c_{ss}^2(2+M+N)}\right]^N\left(\frac{\dot{h}}{a\dot{\varepsilon}_0}\right)^M\left(\frac{a}{D\varepsilon_0}\right)^N, \tag{B9}$$

from which it is deduced that the load factor is

$$F = F_{ss}\left[\frac{2(M+N)}{c_{ss}^2(2+M+N)}\right]^N. \tag{B10}$$